Generation of parabolic similaritons in tapered silicon photonic wires: comparison of pulse dynamics at telecom and mid-infrared wavelengths

Spyros Lavdas,[1,*] Jeffrey B. Driscoll,[2] Hongyi Jiang,[1] Richard R. Grote,[2]
Richard M. Osgood, Jr.,[2] and Nicolae C. Panoiu[1]

[1]*Department of Electronic and Electrical Engineering, University College London, Torrington Place, London WC1E 7JE, UK*

[2]*Microelectronics Sciences Laboratories, Columbia University, New York, New York 10027, USA*

Corresponding author: s.lavdas@ucl.ac.uk

We study the generation of parabolic self-similar optical pulses in tapered Si photonic nanowires (Si-PhNWs) at both telecom ($\lambda = 1.55\ \mu m$) and mid-infrared ($\lambda = 2.2\ \mu m$) wavelengths. Our computational study is based on a rigorous theoretical model, which fully describes the influence of linear and nonlinear optical effects on pulse propagation in Si-PhNWs with arbitrarily varying width. Numerical simulations demonstrate that, in the normal dispersion regime, optical pulses evolve naturally into parabolic pulses upon propagation in millimeter-long tapered Si-PhNWs, with the efficiency of this pulse-reshaping process being strongly dependent on the spectral and pulse parameter regime in which the device operates, as well as the particular shape of the Si-PhNWs.   © 2013 Optical Society of America

OCIS codes: (130.4310) Nonlinear; (230.4320) Nonlinear optical devices; (230.7380) Waveguides, channeled; (190.4360) Nonlinear optics, devices; (320.5540) Pulse shaping.

http://dx.doi.org/10.1364/OL.38.003953

Generation of pulses with specific spectral and temporal characteristics is a key functionality needed in many applications in ultrafast optics, optical signal processing, and optical communications. One type of such pulses are those that preserve their shape upon propagation. Solitons are the most ubiquitous example of such a pulse that forms in the anomalous group-velocity dispersion (GVD) regime, whereas their counterpart in the normal GVD region are self-similar pulses, called similaritons [1–3]. Unlike solitons, which require a threshold power, no constraints have to be imposed on the pulse energy, initial shape, or optical phase profile to generate similaritons. Due to their self-similar propagation, similaritons do not undergo wave breaking and the linear chirp they acquire during their formation makes it easy to employ dispersive pulse compression techniques to generate nearly transform-limited pulses. These remarkable properties of similaritons have provided a strong incentive for their study, and optical similaritons have been demonstrated in active optical fiber systems such as Yb-doped fiber amplifiers [3,4], using passive schemes based on dispersion-managed or tapered silica fibers [5–8], and high-power fiber amplifiers [9–11].

Driven by the ever growing demand for enhanced integration of complex optoelectronic architectures that process increasing amounts of data, finding efficient ways to extend the regime of self-similar pulse propagation to chip-scale photonic devices is becoming more pressing. One promising approach, based on silicon (Si) fibers with micrometer-size core dimensions [12], has been proposed recently [13]. A further degree of device integration can be achieved by employing Si photonic nanowires (Si-PhNWs) of submicrometer transverse size fabricated on a silicon-on-insulator material system [14]. In addition to the enhanced optical nonlinearity, which allows increased device integration, Si-PhNWs allow seamless integration with complementary metal oxide semiconductor technologies. The use of Si-PhNWs can be extended to the mid-infrared (mid-IR) region ($\lambda \gtrsim 2.2\ \mu m$) [15], where Si provides superior functionality due to low two-photon absorption (TPA) and thus reduced free-carrier (FC) absorption. In fact, it has already been shown that nonlinear optical effects such as modulational instability [16,17], frequency dispersion of the nonlinearity [18], and supercontinuum generation [17,19–21] can be used to achieve significant pulse reshaping in millimeter-long Si-PhNWs (for a review, see [22]).

In this Letter, we use a rigorous theoretical model, which describes the propagation of pulses in Si-PhNWs, and comprehensive numerical simulations to demonstrate that optical similaritons with a parabolic shape can be generated in millimeter-long, dispersion-engineered Si-PhNWs. In order to gain a better understanding of the underlying physics of similariton generation, we present a comparative analysis of the pulse dynamics in two spectral domains relevant for technological applications, namely telecom ($\lambda = 1.55\ \mu m$) and mid-IR ($\lambda = 2.2\ \mu m$) spectral regions. Thus, the pulse dynamics are described by the following equation [18,23–25]:

$$i\frac{\partial u}{\partial z} + \sum_{n=1}^{3}\frac{i^n\beta_n(z)}{n!}\frac{\partial^n u}{\partial t^n} = -\frac{ic\kappa(z)}{2nv_g(z)}\alpha_{FC}(z)u$$

$$-\frac{\omega\kappa(z)}{nv_g(z)}\delta n_{FC}(z)u$$

$$-\gamma(z)\left[1 + i\tau(z)\frac{\partial}{\partial t}\right]|u|^2 u, \quad (1)$$

where $u(z,t)$ is the pulse envelope, measured in $\sqrt{W}$; z and t are the distance along the Si-PhNW and time, respectively; $\beta_n(z) = d^n\beta/d\omega^n$ is the nth-order dispersion coefficient; $\kappa(z)$ quantifies the overlap between the optical mode and the active area of the waveguide; $v_g(z)$ is

the group velocity; and $\delta n_{FC}(z)$ and $\alpha_{FC}(z)$ are the FC-induced index changes (losses), which are calculated as $\delta n_{FC}(z) = -e^2/2\epsilon_0 n\omega^2[N(z)/m_{ce}^* + N(z)^{0.8}/m_{ch}^*]$ and $\alpha_{FC}(z) = e^3N(z)/\epsilon_0 cn\omega^2(1/\mu_e m_{ce}^{*2} + 1/\mu_h m_{ch}^{*2})$, respectively, where N is the FC density, $m_{ce}^* = 0.26m_0$ ($m_{ch}^* = 0.39m_0$) is the electron (hole) effective mass, with m_0 the electron mass, and μ_e (μ_h) is the electron (hole) mobility. The nonlinear properties of the waveguide are described by the nonlinear coefficient, $\gamma(z) = 3\omega\Gamma(z)/4\epsilon_0 A(z)v_g^2(z)$, and the shock time scale, i.e., the characteristic response time of the nonlinearity, $\tau(z) = \partial \ln \gamma(z)/\partial\omega$, where $A(z)$ and $\Gamma(z)$ are the cross-sectional area and the effective third-order susceptibility of the waveguide, respectively. Nonlinear optical effects higher than the third order are not considered here, although they might become important at high peak power. Our model is completed by a rate equation for the FC density,

$$\frac{\partial N}{\partial t} = -\frac{N}{t_c} + \frac{3\Gamma''(z)}{4\epsilon_0 \hbar A^2(z)v_g^2(z)}|u|^4, \quad (2)$$

where Γ'' (Γ') is the imaginary (real) part of Γ and t_c is the FC recombination time (in this work, $t_c = 1$ ns).

The system (1)–(2) provides a rigorous description of pulse propagation in Si-PhNWs with adiabatically varying transverse size since the z-dependence of the waveguide parameters is fully incorporated in our model via the implicit dependence of the modes of the Si-PhNWs on their transverse size. Thus, we consider a tapered ridge waveguide with a rectangular Si core buried in SiO$_2$, with height $h = 250$ nm and width, w, varying from w_{in} to w_{out} between the input and output facets, respectively. Using a finite-element mode solver, we determine the propagation constant, $\beta(\lambda)$, and the fundamental TE-like mode, for 1.3 μm $\leq \lambda \leq 2.3$ μm and for 51 values of the waveguide width ranging from 500 to 1500 nm. The dispersion coefficients are calculated by fitting $\beta(\lambda)$ with a 12th-order polynomial and subsequently calculating the derivatives with respect to ω. Alternatively, direct numerical differentiation can be used [26]. Using these results and the optical modes, the parameters, κ, γ, and τ, are computed for all values of w. Their z-dependence is then found by polynomial interpolation.

The results of this analysis are summarized in Fig. 1, where we have plotted the dispersion maps of the waveguide parameters. Thus, Fig. 1(a) shows that if $w < 887$ nm, the Si-PhNW has two zero GVD wavelengths, defined by $\beta_2(\lambda, w) = 0$, whereas if $w > 887$ nm, the Si-PhNW has normal GVD in the entire spectral domain. In addition, if $\lambda > 2187$ nm, the waveguide has normal GVD for any w. Important properties of the Si-PhNW are revealed by the dispersion maps of the nonlinear coefficients as well. Specifically, the strength of the nonlinearity, $\gamma'(\lambda, w)$, decreases with both increasing w and λ, meaning that in the range of wavelengths and waveguide widths explored here, nonlinear effects in Si-PhNWs are stronger if narrow waveguides are used at lower wavelengths. On the other hand, the TPA coefficient, $\gamma''(\lambda, w)$, and consequently nonlinear losses, decrease with w and λ, which suggests that the waveguide parameters and wavelength must be chosen properly for optimum device operation. Finally, as shown in Fig. 1(e),
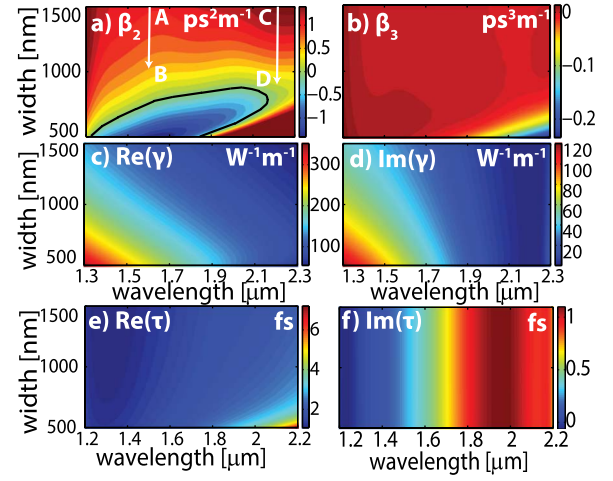

Fig. 1. Dispersion maps of (a) GVD coefficient, β_2; (b) third-order dispersion coefficient, β_3; (c) self-phase modulation coefficient, γ'; (d) TPA coefficient, γ''; (e) the real and (f) the imaginary part of the shock time, τ. In (a), $\beta_2 = 0$ on the black contour and the arrows indicate the limits of w, at $\lambda = 1.55$ and 2.2 μm.

the shock time $\tau'(\lambda, w)$ has large values at long wavelengths, but decreases with w.

To investigate the formation of self-similar pulses, we first consider a Gaussian pulse, $u(t) = \sqrt{P_0}e^{-t^2/2T_0^2}$ with full width at half-maximum (FWHM) $T_{FWHM} = 220$ fs ($T_{FWHM} = 1.665T_0$) and peak power $P_0 = 7$ W, which is launched in an exponentially tapered Si-PhNW, $w(z) = w_{in}e^{-az}$, with $w_{in} = 1500$ nm. The remaining parameters are (i) at $\lambda = 1.55$ μm, $w_{out} = 1080$ nm, $\beta_{2,in} = 1.11$ ps^2 m^{-1}, $\beta_{2,out} = 0.79$ ps^2 m^{-1}, and length $L = 3.5$ mm [arrow A–B in Fig. 1(a)] and (ii) at $\lambda = 2.2$ μm, $w_{out} = 850$ nm, $\beta_{2,in} = 1.53$ ps^2 m^{-1}, $\beta_{2,out} = 0.088$ ps^2 m^{-1}, and $L = 6$ mm [arrow C–D in Fig. 1(a)]. In Fig. 2 we have plotted the pulse profile and its spectrum, calculated for several values of z. As expected, the pulse decay at $\lambda = 1.55$ μm as compared with $\lambda = 2.2$ μm, due to greater TPA. The stronger nonlinear effects at $\lambda = 2.2$ μm are also revealed by the spectral ripples that start to form at $z \gtrsim 5$ mm (no such modulations are seen at $\lambda = 1.55$ μm). Also, the pulse becomes more asymmetric at $\lambda = 2.2$ μm, due to increased τ [18]. However, the most important phenomenon revealed by Fig. 2 is that at both wavelengths the pulse evolves into a parabolic pulse, $|u_p(t)|^2 = |u_p(t_0)|^2[1 - (t - t_0)^2/T_p^2]$ for $|t - t_0| < T_p$ and $u_p(t) = 0$ otherwise, where $u_p(t_0)$, t_0, and T_p are the amplitude, time shift, and pulse width, respectively.

The generation of parabolic pulses can be quantitatively characterized by the intensity misfit parameter, ε_I, which provides a global measure of how close the pulse profile is to a parabolic pulse; it is defined as follows:

$$\varepsilon_I^2 = \frac{\int [|u(t)|^2 - |u_p(t)|^2]^2 dt}{\int |u(t)|^4 dt}. \quad (3)$$

The insets in Figs. 2(a) and 2(b) show that at both wavelengths there is a certain optimum waveguide length at which ε_I^2 reaches a minimum value, i.e., $\varepsilon_I^2 = 1.67 \times 10^{-3}$ ($\varepsilon_I^2 = 1.57 \times 10^{-3}$) at $\lambda = 2.2$ μm ($\lambda = 1.55$ μm). The small values of ε_I^2 provide clear evidence for the
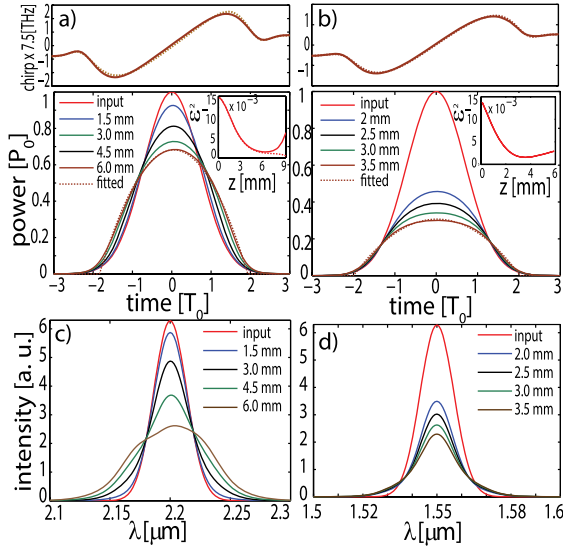
Fig. 2. Temporal pulse shape with increasing z and the chirp of the output pulse, calculated for the full model (solid line) and for $\beta_3 = 0$ and $\tau = 0$ (dotted line) (top panels), and the corresponding pulse spectra (bottom panels). The insets show ε_I^2 versus z, for the full model (solid line) and for $\beta_3 = 0$ and $\tau = 0$ (dotted line). The panels to the left (right) correspond to $\lambda = 2.2$ μm ($\lambda = 1.55$ μm).

formation of parabolic pulses. The pulse becomes closer to a parabolic pulse at $\lambda = 1.55$ μm because the effects that induce pulse asymmetry are smaller at this wavelength. This can also be seen by comparing the dependence $\varepsilon_I^2(z)$ in the case of the full model (1)–(2) and when higher-order effects are neglected ($\beta_3 = 0$ and $\tau = 0$). Thus, at $\lambda = 1.55$ μm, $\varepsilon_I^2(z)$ is almost unaffected if one neglects these effects, whereas under the same conditions, at $\lambda = 2.2$ μm, the minimum value of $\varepsilon_I^2(z)$ decreases considerably to 0.41×10^{-3} (and is reached at $z = 9.52$ mm).

A fundamental characteristic of parabolic pulses is that the frequency chirp varies linearly with time across the pulse. The pulses generated in our numerical experiments clearly have this property, as illustrated in the top panels in Figs. 2(a) and 2(b). These figures also show that, at both wavelengths, this linear time dependence of the chirp is preserved even in the presence of higher-order effects, which demonstrates the robustness against perturbations in the parabolic pulse generation.

The dependence of the similariton generation on the pulse parameters is particularly important when assessing the effectiveness of this optical process. In order to study this dependence, we have determined ε_I^2, at both wavelengths, as a function of pulse parameters T_{FWHM} and P_0. The results of our analysis, summarized in Fig. 3, show that, for a given waveguide length, there is an optimum power at which ε_I^2 reaches a minimum, which is explained by the fact that the similariton formation length increases with P_0. By contrast, there is no optimum value of T_{FWHM} at which ε_I^2 becomes minimum.

The relation between the input pulse parameters and the similariton generation can be further explored by considering pulses with different shapes. Our results regarding this dependence are summarized in Fig. 4, where we have plotted the evolution of $\varepsilon_I^2(z)$, determined for varying P_0. As input pulses we considered a Gaussian
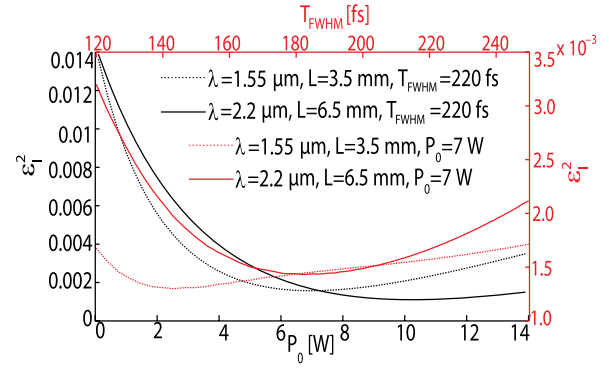

Fig. 3. Dependence of ε_I^2 on pulse width and power.

pulse, a super-Gaussian pulse, $u(t) = \sqrt{P_0} e^{-t^{2m}/2T_0^{2m}}$, with $m = 2$ ($T_{\mathrm{FWHM}} = 1.824 T_0$), and a sech pulse, $u(t) = \sqrt{P_0} \operatorname{sech}(t/T_0)$, where $T_{\mathrm{FWHM}} = 1.763 T_0$. In all cases, $T_{\mathrm{FWHM}} = 220$ fs. There are several revealing conclusions that can be drawn from the maps in Fig. 4. First, the Gaussian pulse leads to the lowest values of $\varepsilon_I^2(z)$, which suggests that this pulse shape is the most efficient one for generating similaritons. Second, in the case of the Gaussian and the sech pulses, there is a band of low values of $\varepsilon_I^2(z)$, which is narrower at $\lambda = 1.55$ μm as compared with $\lambda = 2.2$ μm and in both cases it broadens as P_0 decreases, whereas in the case of the super-Gaussian pulses, two such bands exist. Finally, pulses with a super-Gaussian shape evolve into a similariton over the shortest distance, because among the three pulse profiles, the super-Gaussian profile is closest to a parabolic pulse.

Due to its practical relevance, we also studied the generation of similaritons in Si-PhNW tapers with different profiles. To this end, we considered a linear taper and exponential tapers with different z-variation rates, with the (Gaussian) pulse parameters and w_{in} and w_{out} being the same in all the cases [see Fig. 5(a)]. The results of this analysis, which are presented in Fig. 5, show that, although similaritons are generated irrespective of the taper profile, the efficiency of this process does depend on the shape of the taper. In particular, the linear taper is
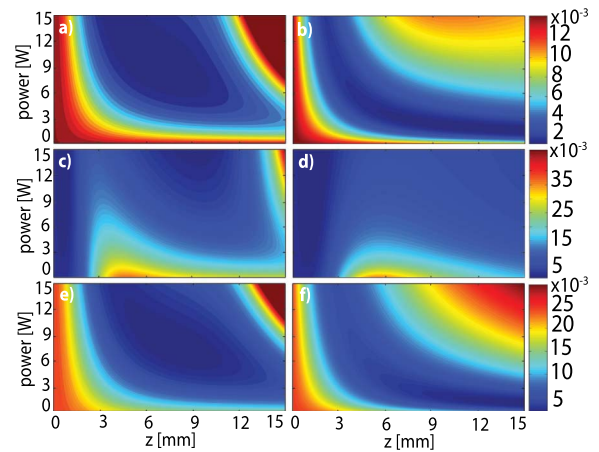

Fig. 4. Dependence of ε_I^2 on z and pulse power, calculated for a Gaussian pulse (top panels), a super-Gaussian pulse with $m = 2$ (middle panels), and a sech pulse (bottom panels). In all cases, $T_{\mathrm{FWHM}} = 220$ fs. The left (right) panels correspond to $\lambda = 2.2$ μm ($\lambda = 1.55$ μm).
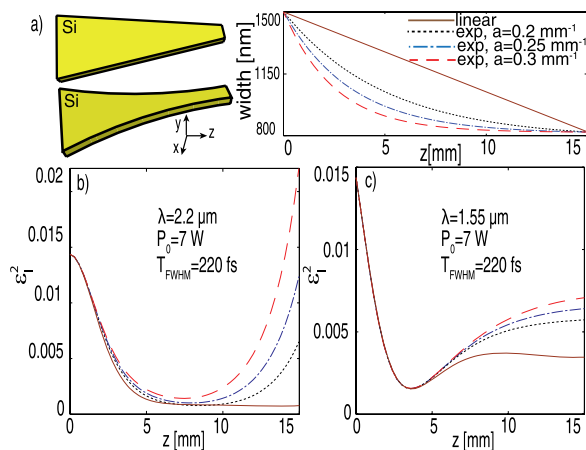
Fig. 5.   (a) Schematics and dependence of $w(z)$ for linear and exponential tapers, $w(z) = w_{in} + [(w_{out} - w_{in})(1 - e^{-az})/(1 - e^{-aL})]$. In all cases, $w_{in} = 1500$ nm and $w_{out} = 820$ nm. Panels (b) and (c) show ε_I^2 versus z for the tapers in (a).

overall the most effective for similariton generation, whereas in the case of exponential tapers, the steeper their profile, the more inefficient they are. These conclusions qualitatively remain valid at both $\lambda = 2.2$ and 1.55 μm, although the overall pulse dynamics do depend on wavelength. In particular, ε_I^2 is smaller at $\lambda = 2.2$ μm and the pulse preserves a parabolic shape over a longer distance, in agreement with the results in Fig. 4.

In conclusion, we have demonstrated that parabolic pulses can be generated in millimeter-long tapered Si-PhNWs with engineered decreasing normal GVD. Our analysis showed that, using this approach optical similaritons can be generated at both telecom and mid-IR wavelengths, irrespective of the pulse shape and taper profile. However, our investigations have revealed that the efficiency of the similariton generation is strongly dependent on the wavelength at which the device operates, the pulse parameters, and its temporal profile, as well as the particular shape of the Si-PhNW taper.

References

1. D. Anderson, M. Desaix, M. Karlsson, M. Lisak, and M. L. Quiroga-Teixeiro, J. Opt. Soc. Am. B **10**, 1185 (1993).
2. K. Tamura and M. Nakazawa, Opt. Lett. **21**, 68 (1996).
3. M. E. Fermann, V. I. Kruglov, B. C. Thomsen, J. M. Dudley, and J. D. Harvey, Phys. Rev. Lett. **84**, 6010 (2000).
4. V. I. Kruglov, A. C. Peacock, J. D. Harvey, and J. M. Dudley, J. Opt. Soc. Am. B **19**, 461 (2002).
5. T. Hirooka and M. Nakazawa, Opt. Lett. **29**, 498 (2004).
6. B. Kibler, C. Billet, P. A. Lacourt, R. Ferriere, L. Larger, and J. M. Dudley, Electron. Lett. **42**, 965 (2006).
7. A. I. Latkin, S. K. Turitsyn, and A. A. Sysoliatin, Opt. Lett. **32**, 331 (2007).
8. C. Finot, L. Provost, P. Petropoulos, and D. J. Richardson, Opt. Express **15**, 852 (2007).
9. J. Limpert, T. Schreiber, T. Clausnitzer, K. Zollner, H. J. Fuchs, E. B. Kley, H. Zellmer, and A. Tunnermann, Opt. Express **10**, 628 (2002).
10. A. Malinowski, A. Piper, J. H. V. Price, K. Furusawa, Y. Jeong, J. Nilsson, and D. J. Richardson, Opt. Lett. **29**, 2073 (2004).
11. S. Lefrancois, C. H. Liu, M. L. Stock, T. S. Sosnowski, A. Galvanauskas, and F. W. Wise, Opt. Lett. **38**, 43 (2013).
12. N. Healy, J. R. Sparks, P. J. A. Sazio, J. V. Badding, and A. C. Peacock, Opt. Express **18**, 7596 (2010).
13. A. Peacock and N. Healy, Opt. Lett. **35**, 1780 (2010).
14. K. K. Lee, D. R. Lim, H. C. Luan, A. Agarwal, J. Foresi, and L. C. Kimerling, Appl. Phys. Lett. **77**, 1617 (2000).
15. R. Soref, Nat. Photonics **4**, 495 (2010).
16. N. C. Panoiu, X. Chen, and R. M. Osgood, Opt. Lett. **31**, 3609 (2006).
17. B. Kuyken, X. P. Liu, R. M. Osgood, R. Baets, G. Roelkens, and W. M. J. Green, Opt. Express **19**, 20172 (2011).
18. N. C. Panoiu, X. Liu, and R. M. Osgood, Opt. Lett. **34**, 947 (2009).
19. O. Boyraz, P. Koonath, V. Raghunathan, and B. Jalali, Opt. Express **12**, 4094 (2004).
20. L. Yin, Q. Lin, and G. P. Agrawal, Opt. Lett. **32**, 391 (2007).
21. I.-W. Hsieh, X. Chen, X. Liu, J. I. Dadap, N. C. Panoiu, C. Y. Chou, F. Xia, W. M. Green, Y. A. Vlasov, and R. M. Osgood, Opt. Express **15**, 15242 (2007).
22. R. M. Osgood, N. C. Panoiu, J. I. Dadap, X. Liu, X. Chen, I.-W. Hsieh, E. Dulkeith, W. M. J. Green, and Y. A. Vlassov, Adv. Opt. Photon. **1**, 162 (2009).
23. X. Chen, N. C. Panoiu, and R. M. Osgood, IEEE J. Sel. Top. Quantum Electron. **42**, 160 (2006).
24. N. C. Panoiu, J. F. McMillan, and C. W. Wong, IEEE J. Sel. Top. Quantum Electron. **16**, 257 (2010).
25. J. B. Driscoll, N. Ophir, R. R. Grote, J. I. Dadap, N. C. Panoiu, K. Bergman, and R. M. Osgood, Opt. Express **20**, 9227 (2012).
26. A. C. Turner, C. Manolatou, B. S. Schmidt, M. Lipson, M. A. Foster, J. E. Sharping, and A. L. Gaeta, Opt. Express **14**, 4357 (2006).